Raman-based mapping and depth-profiling of the relaxation state in amorphous silicon

A.W. Lussier[1], D. Bourbonnais-Sureault[1], M. Chicoine[1], R. Martel[3], L. Martinu[2], S. Roorda[1], F. Schiettekatte[1,*]

[1]Département de physique, Université de Montréal, Montréal, Québec, Canada
[2]Département de génie physique, Polytechnique Montréal, Montréal, Québec, Canada
[3]Département de chimie et Institut Courtois, Université de Montréal, Montréal, Québec, Canada

Abstract – We show that the micro-scale variations in the relaxation state of amorphous silicon (*a*-Si) can be well-identified by Raman mapping over hundreds or thousands of μm^2 in 1-2 hours. Pure and relaxed *a*-Si is obtained by self-implantation in crystalline silicon (*c*-Si) followed by an anneal at 500°C. It is then locally re-implanted over micro-sized patterns to produce unrelaxed *a*-Si zones. Raman mappings are obtained by pointwise confocal μ-Raman and Hyperspectral Raman Imaging (RIMA). We also measure depth profiles of the relaxation state in re-implanted *a*-Si by scanning the edge of a re-implanted sample. We infer from the depth profiles that the minimal damage dose to fully de-relax *a*-Si is 0.04 displacements per atoms, which is an order of magnitude smaller than the fluence needed to fully amorphize *c*-Si.

I. Introduction

In most practical applications of amorphous materials, control of their structure is essential due to the possible variation of their properties on preparation conditions and as a function of deposition time, thus depth [1]. In these materials, Raman spectroscopy is known to probe the local vibrational density of states, which is highly dependent on their local structure [2]. In this work, we explore the use of Raman spectroscopy for lateral and depth-resolved mapping of relaxation state of amorphous materials with a spatial resolution on the order of a micrometer. We do this by applying two different Raman techniques to characterize amorphous silicon in which we have created, using ion irradiation and photolithography techniques, both lateral patterns and a depth profile of ion-induced changes in relaxation state in an otherwise "well-relaxed" matrix. Such regions deliberately brought out of their relaxed state are hereby called "de-relaxed" zones.

Structural properties of amorphous silicon are known to be strongly influenced by its preparation [3] and its thermal treatment [4,5,6]. Studies have shown that thermal treatment below the crystallization temperature (200-500°C) in *a*-Si prepared by Si self-implantation leads to a progressive transition from a fully unrelaxed to the fully relaxed state, the latter being obtained by annealing at 500 °C for ~1 hour. Here, "fully" is used loosely as "fully in the context of this study" since it is nearly always possible to devise a treatment leading to a more relaxed state [7,8,9,10,11]. Conversely, self-implantation in relaxed *a*-Si leads to a progressive evolution from the relaxed to unrelaxed state [2], the state of maximum unrelaxation being reached, in principle, after self-implantation at sufficient fluence and at 0 K [11]. The position of the transverse optical (TO)-like peak [2,12], the width of the TO-like peak [2,12], and the ratio of the area of the transverse acoustic (TA) to the TO-like peaks [12] are linked to the relaxation state of *a*-Si. The narrowing of the TO-like peak width has been associated to a decrease in the bond angle distortion [13, 14] between nearest neighbors in *a*-Si and with a release of stored energy [2, 11], whereas an increase in its frequency and amplitude has also been associated to this distortion [12]. Similar effects have also

* Corresponding author : francois.schiettekatte@umontreal.ca

been observed in Zr-doped Ta_2O_5 [15], which was a potential candidate to replace the current mirrors of LIGO a gravitational wave detector. One motivation for this paper is that *a*-Si is also considered as an alternative to the current mirrors of LIGO and that its relaxation through annealing, which we studied here, could be key in better understanding and lowering its internal mechanical dissipation [16,17,18,19]. Additionally, it has also been shown that stress in *a*-Si:H changes the TO-like peak position [20], much like in crystalline silicon (*c*-Si) [21]. Therefore being able to measure precisely the position of the peak over large areas can also serve as a stress mapping tool in amorphous materials. Examples in litterature present mapping of the strain and changes near micro-indentation marks as a function of loading in *a*-Si [22].

Here, using self-implanted *a*-Si as a test case, we show how the relaxation state of amorphous materials can be imaged over relatively large surfaces, and as a function of depth, in a reasonable amount of time. This provides a tool to probe the homogeneity of the properties of amorphous layers after their deposition or following post-treatments.

2. Experimental

2.1 Preparation of relaxation-patterned and relaxation-depth-profiled *a*-Si layers

A relaxation-patterned sample was fabricated as follows: A 2 µm-thick *a*-Si layer was produced by self-implantation of Si ions at 0.5, 1, and 2 MeV, at 7° of incidence with respect to the <001> orientation of a *c*-Si sample, while the sample holder was cooled with liquid nitrogen (LN_2). The fluence, 50 Si/nm^2 at each implantation energy, guarantees at least 1 displacement per atom (DPA) to amorphize completely a 2 µm-thick layer [2]. The sample was then annealed in a quartz tube

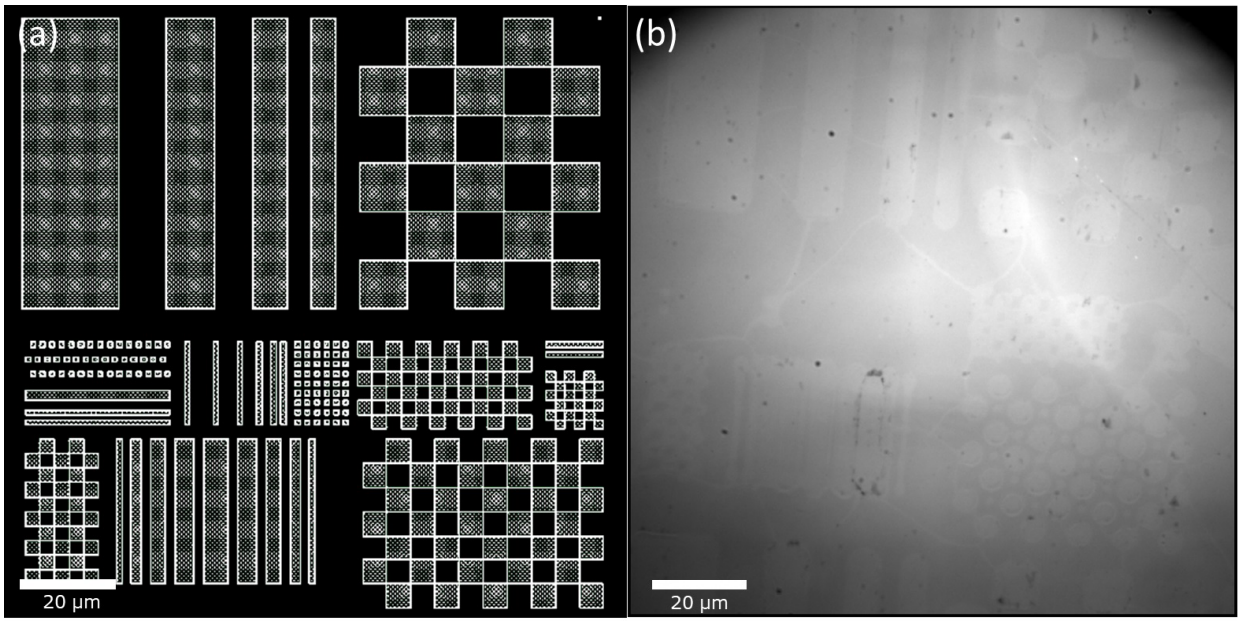

Fig.1: a) Photolithography mask design. b) White light image of the relaxation-patterned sample observed through the RIMA optical microscope. The darker regions are the still-relaxed parts, whereas the brighter part are the re-implanted zones.

furnace at 500 °C for 1 hour at atmospheric pressure with a flux of 500 sccm of N_2 to fully relax the *a*-Si. We then used photolithography to produce a mask through which we performed local re-implantations. More precisely, we deposited a 3 µm thick positive photoresist by spin coating on the sample, and exposed it to UV through a mask (Fig. 1a) and developed the photoresist to leave a pattern featuring multiple holes and lines from 1 to 60 µm in size. We then re-implanted Si ions at 500 keV with a fluence of 15 Si/nm^2 at LN_2 temperature. In this paper, this is referred to as the "fully unrelaxed" state *a*-Si, although further de-relaxation could in principle be obtained by such implantation at 0 K [11]. The energy was chosen so that it damages the top 0.8 µm of the 2 µm *a*-Si layer where the photoresist is removed, while the Si ions stop in the photoresist elsewhere. The photoresist was then removed by reactive ion etching (RIE) with an O_2 plasma. We therefore obtained micro-sized de-relaxed zones in an otherwise fully-relaxed *a*-Si layer according to the photomask pattern chosen. Figure 1b) shows an optical image of the resulting pattern which arises because a change in refractive index between the unrelaxed spots and the relaxed ones [23] changes the reflectivity. It can be seen that most features bigger than 10 µm were developed and implanted correctly, whereas every feature below 5 µm was either absent, deformed or smeared. By comparing the bottom right of both panels of Fig. 1, we can see for example that the checkerboard, consisting of 5 µm squares, resulted in a series of circular unrelaxed zones 5 µm in diameter. Additionally, we observe an implanted spot in between these circles. This is likely due to the photoresist patterns restructuring upon ion implantation. The deposition of a thick metallic layer by evaporation on the photoresist would have prevented such effect, but might have been difficult to remove completely.

Then a series of samples featuring relaxation depth profiles were prepared. For that, a second *a*-Si layer was produced using the same method as for the patterned one, but this time, we performed twelve Si implantations (10 Si/nm^2 at 0.5 and 1 MeV and then from 2 to 20 MeV by steps of 2 MeV at LN_2 temperature) into a *c*-Si sample to achieve an 8 µm-thick layer of *a*-Si. This sample was then annealed the same way as for the previous sample, which resulted in a relaxed layer of *a*-Si. This sample was then split in 4 parts, each of which was re-implanted with Si at a single energy, 8 MeV, still at an angle of 7° of incidence from the sample normal, with the following fluences: 0.5, 1.0, 5, and 10 Si/nm^2, in order to achieve various levels and depth profiles of relaxation. To measure this depth profile, we prepared a cross-section of each sample by cutting them in half, gluing them together with epoxy, and polishing the edge of such stacks to obtain a mirror finish. The final polishing step was achieved using a colloidal suspension of 20 to 60 nm silica particles.

2.2 Confocal µ-Raman mappings and depth-profiling

For µ-Raman mappings, we used a confocal Raman microscope Model inVia Reflex fabricated by Renishaw [24] equipped with a 514.5 nm laser and a 50x objective lens focusing the laser on a ~1 µm diameter spot. The laser power was limited to 1.5 mW to avoid heating damage or unintentional relaxation [25]. The mapping on locally re-implanted *a*-Si (patterned sample) is over a zone of 14 x 60 µm^2. Measurements are spaced by 1 µm and each lasted 10 s. Line map measurements were conducted on the polished edge of the second series of samples. Again, the measurements are spaced by 1 µm, but the line makes an angle of 35° with respect to the sample surface, as illustrated in Fig. 2, which means they were effectively spaced by 0.6 µm along the surface normal, providing more (but overlapping) measurements along the depth.

2.3 Hyperspectral Raman Imaging

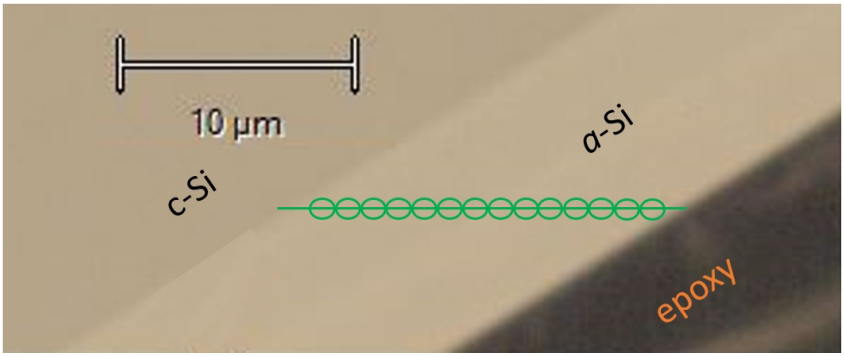

Fig. 2. Optical micrograph showing the cross-section scan achieved to obtain a relaxation depth profile. The green line represents the line along which the scan is carried out, and the green circles represent the laser spot at each measurement, green spots not to scale. The epoxy on top of the *a*-Si layer and the *c*-Si substrate are identified.

The Hyperspectral Raman Imager (RIMA, from Photon Etc.) [26] consists in irradiating a sample surface with a laser beam at 532 nm through a 100× objective lens with a numerical aperture of 0.9, focusing it on a 133 × 133 µm^2 spot on the sample. The laser power, of up to 4 W, is maintained relatively constant over several hours. The signal coming from the (x, y) position on the sample passes through a Bragg tunable filter that selects only one wavelength per position. This wavelength changes along the x axis. The spectra are collected on a 1024 × 1024 pixels CCD with each pixel measuring a corresponding sample spot of 130 × 130 nm^2. To measure the full spectrum at each (x, y) position, the angle of the Bragg filter is scanned to change the central wavelength of the image. By shifting and superimposing multiple map/spectra, one can reconstruct the spectrum at each (x, y) position, as detailed in Ref. 26. The technique was applied to the patterned *a*-Si sample. The laser power, in our case 3.25 W, of which only 325 mW gets to the sample, yields a power flux of 0.019 mW/µm^2, which is two orders of magnitude lower than for the confocal µ-Raman measurements.

3. Results and discussions

In this Section, we first present the results regarding the depth profiling of the relaxation state of *a*-Si (profiled sample) using µ-Raman spectroscopy, and then the mapping of the relaxation state over the relaxation-patterned sample, using both µ-Raman and RIMA.

3.1 µ-Raman relaxation depth-profiling

Figure 3 shows examples of µ-Raman spectra obtained from two pieces of *a*-Si: re-implanted (orange) and relaxed (blue), and normalized to the TA-like peak so that they have the same area. The different vibrational modes are indicated. We see that the TO-like peak shifts and decreases in intensity upon re-implantation, and that its half-width at half maximum (HWHM) increases. In order to extract information about the TO-like peak position (ω_{TO}) and width (Γ_{TO}), we fit the spectra to 3 Gaussian distributions (9 parameters) associated to the TO-like, longitudinal acoustic

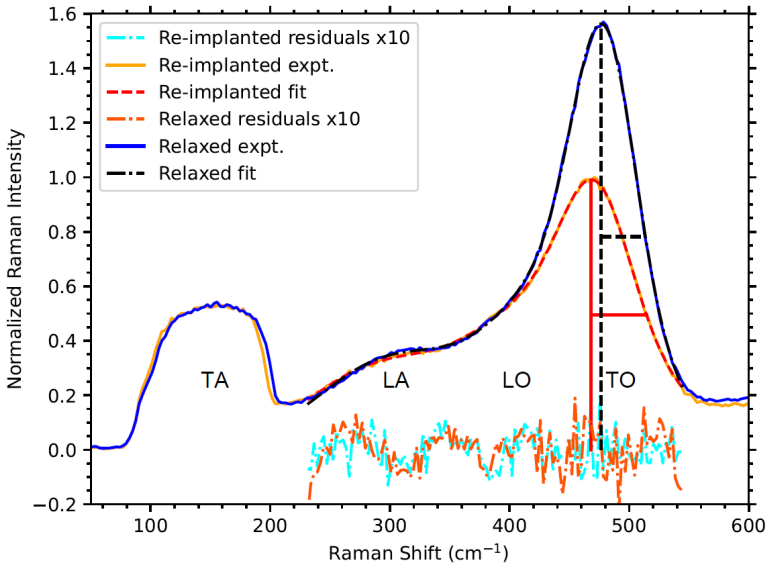

Fig. 3. μ-Raman spectra of re-implanted (light orange) and relaxed *a*-Si (dark blue), their respective fits, peak half-width and position in red and black. μ-Raman spectra acquired during 10 min. The different vibrational mode peaks are identified, as well as the position and HWHM of the TO-like peaks (thick lines). The residuals ×10 are shown for re-implanted (dark orange) and relaxed (light blue).

(LA-like) and longitudinal optic (LO-like) peaks in the range between 231 and 545 cm^{-1}. The resulting smooth spectrum is used to extract ω_{TO}. Γ_{TO} is computed using the high-wavenumber edge of the TO-like peak. Note that the half-maximum is taken from the total signal without subtracting a background that would, for example, account for the signal observed above 550 cm^{-1}, as it is in principle part of the Raman signal.

To get the TA/TO peak ratios, we simply integrated the raw spectra from 100 to 200 cm^{-1} and divided by the total integrated intensity from 400 to 545 cm^{-1}. The first interval is chosen such that it corresponds to the TA peak intensity and is almost unchanged by the relaxation. The second interval is chosen to achieve the highest contrast between relaxed and unrelaxed material.

For the depth profiles, we had to adjust the fitting procedure to subtract the epoxy contributions from the top surface of the sample, and that of the *c*-Si close to the *a*-Si/*c*-Si interface. Indeed, only a small amount of *c*-Si or epoxy signal significantly affects the *a*-Si spectrum. So, corrections to the acquired spectra are then needed, and some measurements, very close to the interfaces, are discarded because the subtraction is not reliable or the detector became saturated during the measurement. As a result, the scans do not cover the full 0-8 μm interval. When a *c*-Si signal is present at 520.5 cm^{-1}, in addition to the 3 Gaussians mentioned previously, we fit a Lorentzian to the *c*-Si peak, although removing the Lorentzian from the raw data does not subtract it perfectly well. Therefore, we integrate the fit of the TO-like peak (i.e., the intensity from the 3 Gaussians) rather than the raw data, which can slightly affect the TA/TO ratio. Also, since the *c*-Si peak is superimposed on the half-maximum of the *a*-Si TO-like peak, it can also affect the Γ_{TO} measurement from the spectrum if the *c*-Si peak amplitude is strong. These considerations are taken into account when estimating the uncertainties of each data.

In Fig. 4, we plot ω_{TO} as a function of depth for the relaxed *a*-Si samples re-implanted with 8 MeV Si at indicated fluences. For larger fluences, 5 and 10 Si/nm^2, we observe that the implanted depth (first 4 μm) features values of about 467 cm^{-1}, typical of fully unrelaxed *a*-Si [27]. This is followed by a sharp transition, over about 1 μm, to a value of about 475 cm^{-1} [28], the remainder of the depth profile featuring such values since 8 MeV Si does not reach these depths. For lower fluences, 0.5 and 1.0 Si/nm^2, we see that over the first 5 μm, ω_{TO} remains at intermediate values, indicating that *a*-Si is partially relaxed. At deeper depths, ω_{TO} stays at values typical of relaxed *a*-Si, as it was the case for higher fluences. We therefore observe a relaxation state depth profile. It differs from the samples implanted at higher fluences where de-relaxation reached a saturation value in the first 4 μm. We rather see a minimum value of ω_{TO} near 4 μm. As we will see below, this corresponds to the depth where the number of DPA reaches its maximum value. The minimum value of ω_{TO} depends on the fluence of implantation. For the sample re-implanted with 0.5 Si/nm^2, it reaches 471 cm^{-1} compared to 468 cm^{-1} for the one at 1.0 Si/nm^2, which is close to the saturation value reached at higher fluences. Very similar observations come out of the depth profiles of the TA/TO ratio and Γ_{TO} (not shown).

In Fig. 4 e), we show the DPA depth profile after an implantation of 10 Si/nm^2 at 8 MeV according to a SRIM (Stopping and Range of Ions in Matter) simulation (orange curve) [29], and its convolution considering a Gaussian laser beam with $\sigma = 0.5$ μm (blue curve). Then, for each depth of each profile, we plot in Fig. 5 the value of an observed Raman features (a) ω_{TO}, b) the TA/TO peak ratio, and c) Γ_{TO} as a function of the DPA according to the convoluted curve of Fig. 4e) at that same depth. With this, we are able to get a relation between the DPA and the value of each Raman feature.

Some literature discusses a process by which, during implantation, each implanted atom melts a zone [30] that solidifies back and creates a local de-relaxation pocket along its track. In previous work, some of the authors have shown that, while not melting the material, primary recoils in *a*-Si produce de-relaxed zones [31]. However, if the environment of an atom has already been significantly disturbed, a second or third impact (and so on) should not further de-relax the material [11]. Therefore, if we assume that the Raman features are a proxy for the relaxation state, their value should evolve as the probability for an atom of having been displaced at least once. Hence, we expect the relation between Raman features and DPA (which, in our case, is a function of the depth, x, in the layer) to follow a scaled Poisson probability, $1 - P_0$, that at least one atom was displaced, i.e.:

$$F(DPA(x)) = a(1 - \exp(-DPA(x)\, n)) + b \qquad (1)$$

where F is the value of a given Raman feature, a is the Raman feature value change when *a*-Si goes from relaxed to unrelaxed, n is a factor that we will discuss below, and b is the value of the Raman feature when *a*-Si is fully relaxed. Knowing the DPA as a function of depth from Fig. 4e), we convert the depth scale Fig. 4a) to d) to a DPA scale and report the values in Fig. 5a). The same is done regarding the TA/TO peak area ratio and the value of Γ_{TO}, and the results are reported in Fig. 5b and c), respectively. Equation 1 is fitted to each feature's data (solid blue line) and the fitting parameters are found in Tab. 1. Considering the factor n, Tab. 1 shows that its value remains similar, 26±6, across the different Raman features. (The uncertainty on this value also takes into account the uncertainty on the laser beam radius.) It therefore indicates that the characteristic DPA

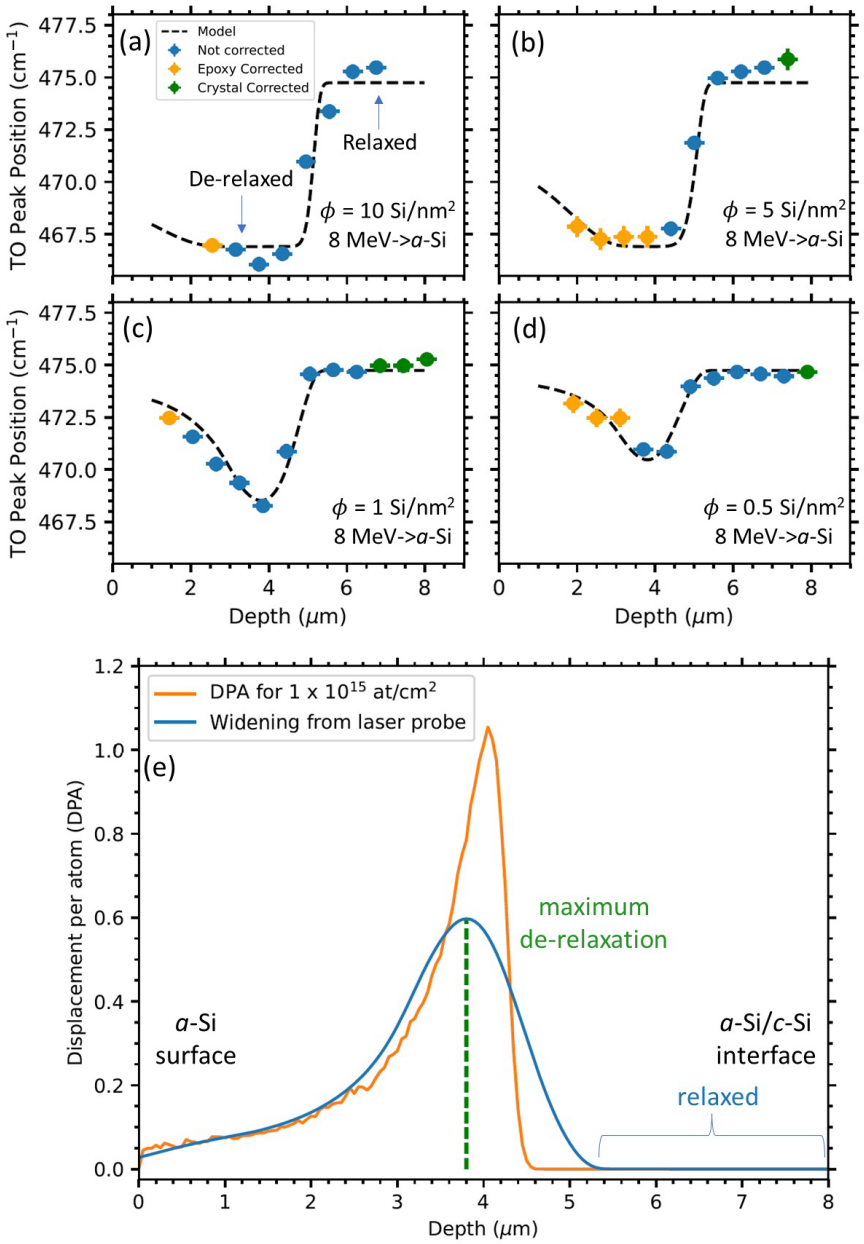

Fig. 4. TO-like peak position (ω_{TO}) depth profiles for fully relaxed *a*-Si re-implanted with 8 MeV Si ions at fluences of a) 10, b) 5, c) 1.0, and d) 0.5 Si/nm^2, respectively. The blue points are from spectra that did not need subtraction for epoxy or *c*-Si, whereas the orange and green points are from spectra which required subtraction of an epoxy and *c*-Si signal contribution, respectively. The black dashed curves are modelled based on the damage profile in e) where the vertical axis is computed using the reciprocal of Eq. 1 with parameters from Tab. 1 (see text). e) DPA depth profile considering a fluence of 10 Si/nm^2 at 8 MeV (orange), according to a SRIM simulation. The blue curve is the same profile convoluted by Gaussian with a standard deviation of 0.5 µm, corresponding to the radius of the laser beam.

to fully de-relax *a*-Si is 0.04, or more specifically, that 0.04 DPA is sufficient to bring *a*-Si to $1/e$ of its fully unrelaxed state, slightly above the value found by Roorda *et al.* [2]. Interpreting the

integrated heat flow of self-reimplanted a-Si from [11] indicates that a-Si releases $1 - 1/e$ of its maximal integrated heat flow at approximately 0.07 DPA when implanted at 133 K and of approximately 0.03 DPA when implanted at 297 K, in relative agreement with what we measured. This is an order of magnitude smaller than the fluence needed to fully amorphize c-Si [32]. Taking a step further in the interpretation of this value, since n has units of atoms/displacement, we can interpret its value as if a single displacement fully de-relax 26 atoms in a-Si on average. Simulation work also showed comparable damage accumulation following self-implantation in a-Si [31].

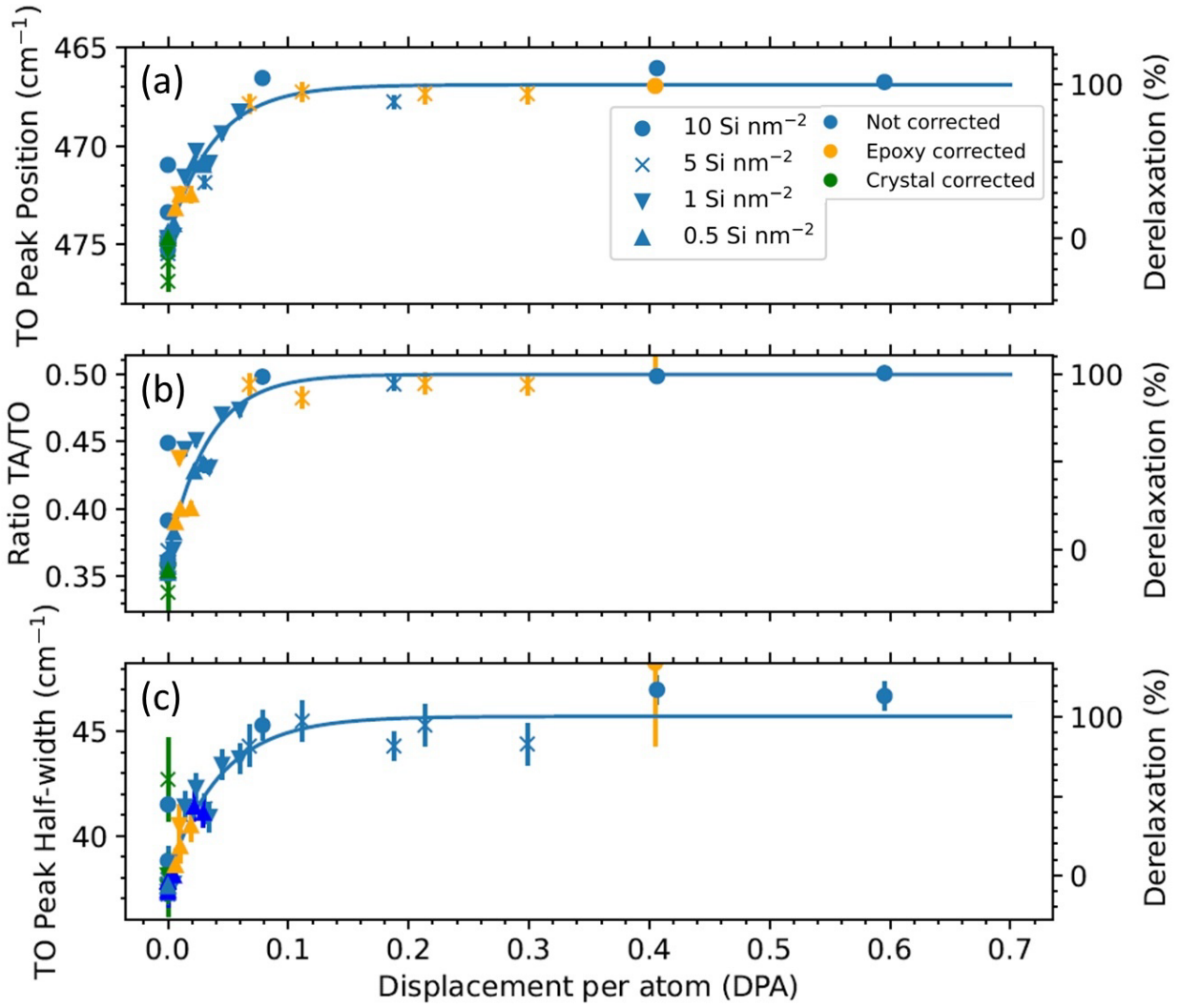

Fig. 5. Raman features value as a function of the DPA at the corresponding depth. a) TO-like peak position (ω_{TO}). b) TA/TO peak ratio. c) TO-like peak half-width (Γ_{TO}). Data point color code shown in panel a). Symbols indicated the re-implanted fluence: circles for 10 Si/nm^2, crosses for 5 Si/nm^2, down-pointing triangles for 1.0 Si/nm^2, and up-pointing triangles for 0.5 Si/nm^2. The blue curves are a fit of Eq. (1), where the parameters can be found in Tab. 1. For reference, the right axis represents the derelaxation between 0% and 100%, deduced from the minimum to the maximum value of Eq. (1) for each Raman feature.

Using the values in Tab. 1 in Eq. (1), we can convert the vertical axis of the convoluted damage depth profile in Fig. 4e) (blue curve) into the corresponding $\omega_{TO}(x)$. This is the model represented as a dashed curve in Fig. 4a). The method is applied to damage depth profiles of correspondingly lower amplitude for lower fluences, and also plotted as dashed lines in Fig. 4b), c) and d). We see that the model reproduces very well the ω_{TO} depth profile, further validating that Raman can be used as a relaxation state depth profiling technique.

Table 1: Value of the parameter of Eq. 1 fitted to the data points in Fig. 5.

	a	n	b (value for relaxed a-Si)	a + b (value for fully-unrelaxed a-Si)
TO position	-7.8±0.7	26±3	474.7±0.5	466.9±0.5
Ratio TA/TO	0.13±0.02	30±3	0.37±0.02	0.50±0.02
TO half-width	7.6±1.0	23±4	38.1±1.0	45.7±1.0

3.2 *Hyperspectral Raman Imaging* of the relaxation state

Now considering relaxation-patterned a-Si layer, using the RIMA setup, we performed two 60-minute measurements: one on the patterned sample, and the other on a uniform amorphous germanium (a-Ge) sample, which is used to determine the background signal (see below). We used a 3 × 3 binning of the data, which means that each pixel has a size of about 0.4 x 0.4 µm^2. The spectrum is acquired from 400 to 560 cm^{-1} to observe the main TO-like peak of a-Si. Due to the limitations of the instrument, we were not able to measure at lower Raman shifts, which would have allowed us to observe the TA peak. Our RIMA spectra also feature a strong background (signal:background ~1:90), which makes it difficult fitting Gaussians as we do with the confocal µ-Raman measurements. Rather, we first subtract the background, and then carry out a 2-component fit.

Let $I(x, y, \lambda)$ be the raw RIMA signal, that is, the measured intensity at a given Raman shift λ and at a given point (x, y) on the surface for an a-Si layer. Likewise, $h(x, y, \lambda)$ is the RIMA signal from an a-Ge layer, which should feature the same background signal, but no Raman feature in the wavenumber range specified. Examples of these two spectra, averaged over the points circled in cyan in Fig. 7b), are presented in Fig. 6a). Therefore, $I(x, y, \lambda) - h(x, y, \lambda)$ represents the background-corrected spectrum of a-Si (Fig. 6b), solid green curve).

On this signal, we carry out a 2-component fit. The 2 components are actually the spectra from Fig. 3, obtained by confocal µ-Raman, fitted by 3 Gaussians, which we call $f(\lambda)$ for the unrelaxed (or re-implanted) a-Si (orange) spectrum, and $g(\lambda)$ for the relaxed a-Si (blue) spectrum. On each point (x, y) of the RIMA data, we adjust our two components to by fitting them to $I(x, y, \lambda) - h(x, y, \lambda)$ with amplitude $a(x, y)$ and $b(x, y)$, respectively, that is, we find:

$$\delta(x, y, \lambda) = min \sum_{\lambda} \left(I(x, y, \lambda) - h(x, y, \lambda) - \tilde{I}(x, y, \lambda) \right)^2 \qquad (2)$$

where

$$\tilde{I}(x, y, \lambda) = a(x, y) f(\lambda) + b(x, y) g(\lambda) - i(\lambda). \qquad (3)$$

An example of $\tilde{I}(\lambda)$ is plotted in Fig. 6b) (yellow dot-dashed curve). Such a spectrum features negative value owing to the fact that we subtracted an *a*-Ge spectrum that had parts of larger amplitude than the *a*-Si spectrum, as seen in Fig. 6a). To compensate for that, we add to the resulting fit a smoothed spectrum $i(\lambda)$, which is a Raman spectrum acquired by confocal μ-Raman spectroscopy from an *a*-Ge layer. The compensated spectrum and fit are represented as the solid red curve and gray dashed curve in Fig. 6c), respectively. Figure 6d) shows the residuals, $\delta(\lambda)$ as a black dashed curve.

By using this fitting procedure on each point (x, y) of the map, we obtain the maps $a(x, y)$ and $b(x, y)$ that show the unrelaxed and relaxed *a*-Si contribution to each spectrum. It does not necessarily allow to assess quantitatively the degree of relaxation of each point (x, y) as seen in Section 3.1, but it should reveal non-uniformities in the relaxation state over large areas. Figure 7a) shows the total intensity integrated over λ, $I(x, y) - h(x, y)$, for our relaxation-patterned sample, while panel b) and c) show the relaxed and unrelaxed components of the fit, $b(x, y)$ and $a(x, y)$, respectively. Figure 7e) presents the normalized line profiles of the relaxed component $b(x, y)$ along the lines of the corresponding color in Fig. 7b), and Fig. 7d) presents the normalized line profiles of the total intensity (boxcar-averaged over 5 pixels) along the same lines. (Note that the horizontal axis in each subgraph is not the same, and that the line profiles are lines averaged over 3 pixels wide.) The black square curve shows the ideal profile, if the photoresist pattern was perfectly sharp, without boxcar average, assuming that the implanted ions went in straight line and, chiefly, if the RIMA measurement featured no noise and a perfect spatial resolution. Figure 7f) shows histograms of the *a* and *b* components taken from zones identified by circles in Fig. 7b), one that should be fully relaxed (purple), and the other that has been re-implanted (cyan). From panels a), b) and c) of Fig. 7, we see that each map can, in their own way, identify the zones that are relaxed and unrelaxed as long as they are bigger than 5 μm. Indeed, in panel e), the red and green line profiles show clear variations in the relaxed and unrelaxed component, which are spaced by 5 μm. To show to which extent the b component map is similar to the intensity map, we compare line profiles taken from these 2 maps (Fig. 7d) and e)). The intensity profiles follow local intensity changes but not to the nominal level, especially for smaller features, as seen in the two bottom graph of Fig. 7e). On the other hand, for the b component profiles (Fig. 7e), we can see relatively sharp drops on a scale of less than 3 μm. In Fig. 7a), we also see a contour around each feature. Its origin is not clear, but it appears to be a diffraction effect. This is not observed in the component images, Fig. 7b) and c). Although it is not very visible in the white light image from Fig. 1b), it can be seen by slightly adjusting the focus.

Figure 7f) shows the purple histograms that are computed from data taken on a relaxed zone. The results show that these points have mostly a relaxed component as the core of the histogram is on the right of the top panel. Very few points feature small $b(x, y)$ values. Conversely, the bottom panel shows that most of the points in the purple area feature an $a(x, y)$, unrelaxed component close to 0. Regarding the cyan circle, which covers a re-implanted area, we see that both histograms

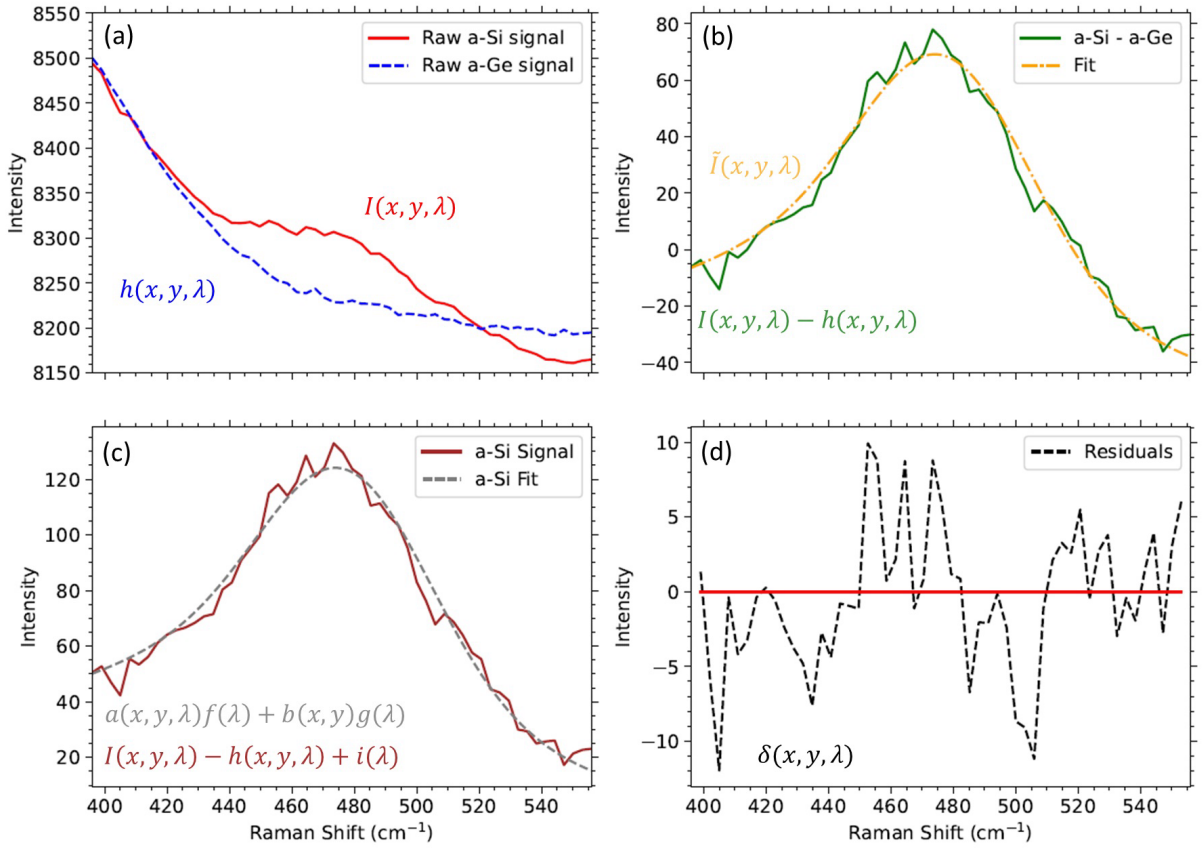

Fig. 6. a) Raw RIMA intensities measured from *a*-Si (red, solid) and *a*-Ge (blue, dashed) averaged over the zone circled in cyan in Fig. 7 b). b) Spectrum from *a*-Si subtracted by the one from *a*-Ge (green, solid), on which is fitted Eq. (3) (yellow, dashed dotted) according to Eq. (2). c) *a*-Si spectrum from panel b) to which a spectrum measured by confocal μ-Raman spectroscopy on *a*-Ge is added (brown, solid). The gray dashed curve shows the result of the 2-component fit. The residuals, $\delta(\lambda)$, are represented in d) by the black dashed curve.

are much wider as these points have a significant contribution from both the relaxed and unrelaxed components. We indeed see that Fig. 7c) shows more speckles in paler shades area, which identify the re-implanted, unrelaxed regions, meaning that some points were fitted with a strong relaxed component. The speckles from Fig. 7b) also produce the fast fluctuations in the line profiles of Fig. 7e).

We can estimate the signal-to-noise ratio (SNR) [33] from the lines in panel e) and from the histogram of panel f). From the lines in panel e), we see that the noise depends on the location but on average, the fluctuation in the data is approximately 1/3 of the nominal signal (black curves); therefore an approximation of the SNR is 3. Considering the histograms, we can compare the distributions average to their width. For the unrelaxed component, we get an SNR of approximately 1.1, while it is 1.4 for the relaxed component. We note that, through spatially averaging (3 pixel wide), the speckle are smoothed out and result in a higher SNR of about 3.

We conclude that our $a(x, y)$ and $b(x, y)$ component mapping can indeed distinguish the relaxed and unrelaxed zones relative to each other on average, even though the noise strongly affects their precision. This noise is likely due to the strong background level and subtraction. Such noise prevents us from directly deducing the TO-like peak position and width as we did in Section 3.1, and rather rely on a 2-component fit. This can also be partially explained by the fact that unrelaxed spectra have lower Raman intensity than the relaxed zones, therefore the signal is noisier, which could lead to more statistical fluctuations and fit misclassification. Speckle and fluctuations also prevent the technique from identifying the relaxation state of individual pixels, but by taking averages, this can be achieved over zones that are bigger than 5 µm, with a spatial resolution of approximately 3 µm, in an hour measurement on a large, 133 x 133 µm^2 area.

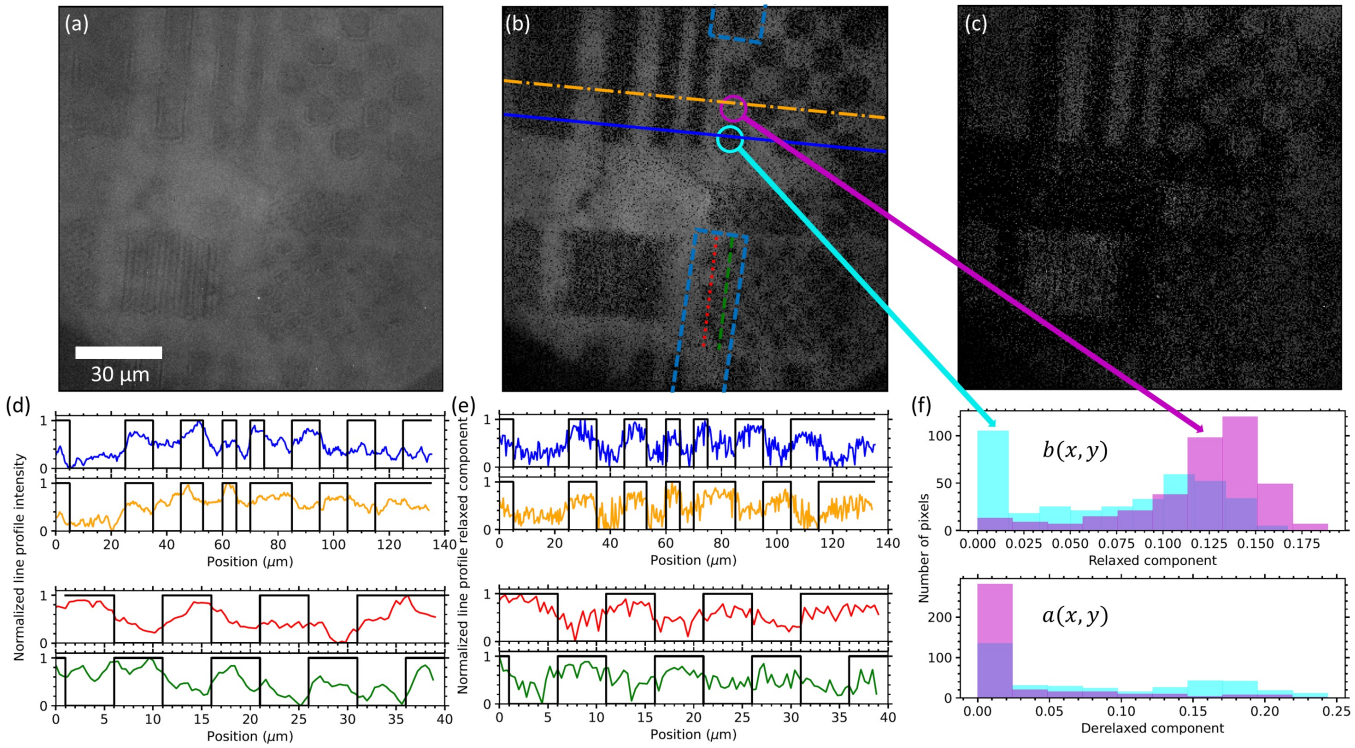

Fig. 7. a) Map of the total intensity, $I(x, y, \lambda) - h(x, y, \lambda)$, integrated over λ. b) Relaxed component from the 2-component fit, $b(x, y)$. Hence, the paler areas are where the material is relaxed while the darker areas are re-implanted, unrelaxed regions. c) Unrelaxed component $a(x, y)$, implanted areas now showing up in paler gray tones. The green, red, yellow and blue lines in panel b) represent the location of the line profiles reported using the corresponding color in panels d) and e). In d), the line profiles are taken from the intensity map (panel a), and are boxcar-averaged over 5 points and 3 pixels in width, while in e), they are taken from the relaxed component map (panel b), and averaged over 3 pixels in width. (Note that the two bottom graphs of these panels cover a smaller range than the two upper ones.)The purple and cyan circled areas in b), covering relaxed and implanted zones, respectively, are used to compute histograms of the $a(x, y)$ and $b(x, y)$ component, presented in panel f). The cyan histograms correspond to each component in the cyan circle, and likewise for the purple ones. The blue dashed rectangle shows the zone mapped in Fig. 8.

3.3 Confocal μ-Raman mappings

In order to compare to RIMA, we carried out confocal μ-Raman mappings on the same samples. Scans were achieved over an area of 64 × 16 μm^2, represented as the blue dashed rectangle on Fig. 7b). The acquisition took 2 hours 30 minutes, i.e. 1.25 times the length of the total RIMA acquisition, but over an area 21 times smaller. In this sense, the comparison is relatively unfair, as the laser power density is much higher and much less noise is expected. Much better SNR would have been achieved during a 48 hours RIMA acquisition, although the stability of the system would have to be monitored closely over such a long period of time.
Panels a), b) and c) of Fig. 8, present maps of Γ_{TO} , ω_{TO} and TA/TO peak ratio, respectively. The values have been determined at each point of the mapping in the same way as in Sec. 3.1. We see that the microscale features are well extracted by this method, since we can clearly observe a 10 μm square and six 5 μm-diameter disks. The three Raman features can distinguish the re-implanted zones from the relaxed ones. Looking at Fig. 8a), we can see that the transitioning between relaxed and unrelaxed zones is relatively sharp, with 1 "mixed" pixel (which is 1 μm wide) between the zones, that pixel featuring an intermediate value between that of the relaxed and unrelaxed values. The sharpness of the transition is also visible from Fig. 8d), which presents a line profile of ω_{TO} taken from Fig. 8b) along the pixel column pointed by an arrow. The sharpness of the feature profile, with variations within 1-2 μm in position, is compatible with the expected resolution, given that the laser spot has a 1 μm diameter. In addition, the profile of ω_{TO} changes over its full value span, from 476 to 468 cm^{-1}, and likewise, that of Γ_{TO} changes from 37 to 45 cm^{-1}, while TA/TO peak ratios go from 0.35 to 0.475 (not shown), in good agreement with the values reported in Tab. 1 and in partial agreement with Ref. 2, who also argues that it corresponds to a change from relaxed to unrelaxed state in *a*-Si. This measurement is therefore much more sensitive to variations than our corresponding RIMA measurement, when it is compared to the line profiles in Fig. 7e). Although we expect from the white light image of Fig. 1b) that, in between the circles, there should be implanted spots, this is below the sensitivity of the method, except perhaps for one location near the middle of the maps.

In order to more accurately assess the capability of the technique to resolve the relaxation state, we plot the histograms in Fig. 8 e), f) and g), which represent the distributions of the values of the parameters in Fig. 8 a), b) and c), respectively, considering the areas marked by red rectangles in Fig. 8c). It shows that the method is sensitive to a ω_{TO} change of about 1 cm^{-1}, much smaller than the interval between the values for fully relaxed and fully unrelaxed material. To assess the SNR, we again take the difference of the average of the two zones divided by the variance of one zone. The values are reported in each histogram. It reaches about 14 for the TO-like peak features, and up to 22 for the TA/TO peak ratio.

A goal of this experiment was to determine the resolution and sensitivity of Raman-based strain mapping by applying it to the well-known relaxed-unrelaxed *a*-Si system. Indeed, we can probe the relaxation state with a sensitivity of ~5% over an area of 1 μm^2. The SNR is much larger than we obtained using RIMA, but over an area 21 times smaller for a comparable acquisition time. To benchmark the results, we compare the SNR in a μ-Raman spectrum from the mapping to the SNR as we combine RIMA pixels. A similar SNR is obtained as we combine between 150 and 530 RIMA 0.4 x 0.4 μm^2 pixels, corresponding to 25-85 μm^2. As the μ-Raman map is approximately

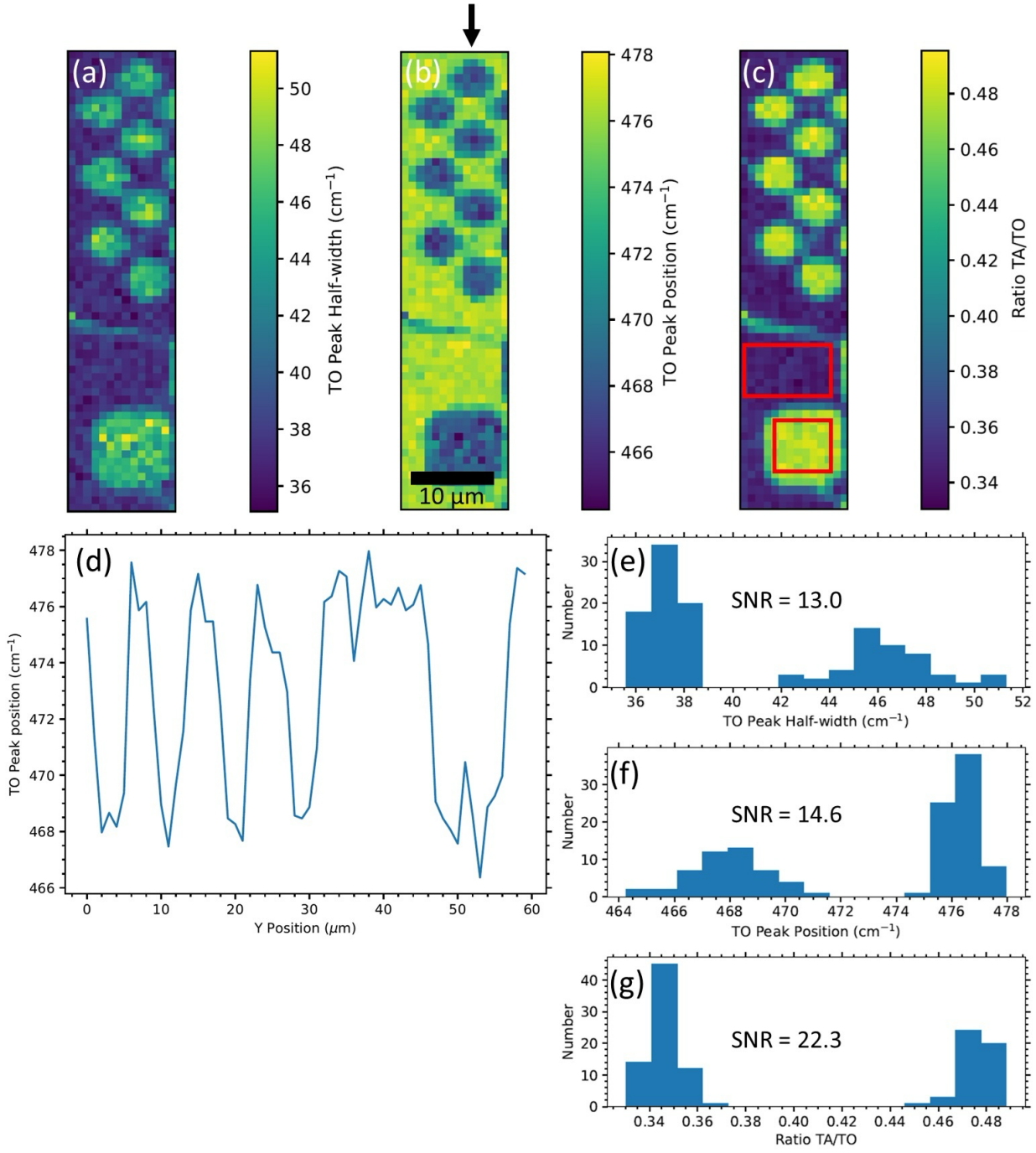

Fig. 8. For the area indicated by a dashed blue rectangle in Fig. 7b), maps of a) the TO-like peak upper half-width, $\Delta\omega_{TO}$, b) the TO-like peak central position, ω_{TO}, and c) TA/TO peak ratio, normalized by the TO-like peak integrated amplitude. Panel d) shows a line profile of ω_{TO} along the vertical axis for the pixel column pointed by an arrow in panel b). Panels e), f) and g) present histograms of the pixels values in a), b), and c), respectively, from zones identified by red rectangles on panel c). The computed SNR is indicated.

21 times smaller than the RIMA map but took 25% more time to acquire, we obtain that for a 1 μm precision mapping that RIMA is between 1 and 3 times worse. The advantage of RIMA is that we can obtain low-resolution maps fast as we don't need to scan the laser and, with long integration time, offers in principle comparable SNR with diffraction-limited spatial resolution and 130 nm binning over such a wide area. RIMA would also become vastly superior if its laser power could be improved, as the power flux is very low while that of μ-Raman is already optimized to avoid heating effects.

Being able to follow the value of ω_{TO} with a ~1cm^{-1} sensitivity opens the door to the fast mappings of the relaxation state and to depth profiling both relaxation and stress. For example, one could look at the influence of H at the micro-scale. Since *a*-Si:H has a lower Young's modulus (80 GPa [34], and dependent on H concentration) than *a*-Si obtained by implantation (140 GPa) [35], a change in stress of, let say, 520 MPa, should yield a change in ω_{TO} of 3.3 cm^{-1}, which should be observable. In their paper, Gerbig *et al*. [22] show that they were able to map strain in a-Si following the application of loads down to 3.5 GPa with already clear changes in ω_{TO}. This parameter would probably have been sensitive to much lower loads, comparable to our estimate. And since a relation between the Raman peak width and the relaxation state has been observed in other materials such as in ZrO_2:Ta_2O_5 [15], it should be possible to extend this relaxation-state mapping method to other amorphous materials and mixtures.

4. Conclusion

We applied two different Raman techniques to characterize amorphous silicon in which we have created, using ion irradiation and photolithography techniques, both lateral patterns and a depth profile of ion damage in an otherwise "well-relaxed" matrix. We showed through μ-Raman mapping and Hyperspectral Raman Imaging (RIMA) that these methods are effective at probing the relaxation state at the micro-scale in *a*-Si. RIMA is effective at carrying out fast measurement over large areas (1.7×10^4 μm^2), and the spectral accuracy only allows to distinguish whether zones of a few μm are relaxed or unrelaxed, whereas over the same amount of time, μ-Raman is able to probe a much smaller area (~10^3 μm^2) but with a spectral accuracy sufficient to probe the relaxation state with a sensitivity of up to 5%, and a better spatial resolution. For longer acquisition times over 133 × 133 μm^2, both techniques should achieve similar SNR over 1 μm^2 but RIMA would measure up to the limit of diffraction. We also showed that confocal μ-Raman can be used for depth-profile analysis of the relaxation state of *a*-Si in re-implanted *a*-Si by scanning few-μm-thick films cross-section. We showed that the technique can probe partial relaxation state as a function of depth with a 5% sensitivity. From these depth profiles, a model allows to infer a damage dose of 0.04 DPA to fully derelax *a*-Si. The result can be interpreted as if each displaced atom derelaxes 26 atoms in the amorphous network. The relation between Raman features and relaxation state and stress having also been observed in other amorphous materials, it should be possible to extend the method to map these other material properties at the microscale.

5. Acknowledgements & Declarations

The authors would like to thank S. Elouatik for his support using the μ-Raman instrument, F. Debris for technical support and maintenance of the accelerators and P. Vinchon for great insight

about the RIMA instrument. We would also like to thank the members of the Optical Working Group of the LIGO Scientific Collaboration for fruitful discussions. This document has been assigned LIGO document number P2300351. The project is supported by a Projet en équipe grant from the Fonds de recherche du Québec – Nature et technologies (FRQNT), it is also supported through the Natural Sciences and Engineering Research Council of Canada (NSERC) Discovery program, using equipment obtained through the NSERC and the Canadian Foundation for Innovation. AL holds a NSERC and FRQNT graduate scholarship. The authors have no conflicts to declare.

Reference

[1] G. Abadias, E. Chason, J. Keckes, M. Sebastiani; G. B. Thompson, E. Barthel, G. L. Doll, C. E. Murray, and C. H. Stoessel, L. Martinu, J. Vac. Sci. Technol. **A 36**, 020801 (2018).
[2] S. Roorda, W. C. Sinke, J. M. Poate, D. C. Jacobson, S. Dierker, B. S. Dennis, D. J. Eaglesham, F. Spaepen, and P. Fuoss, Phys. Rev. **B 44**, 3702 (1991).
[3] P. A. Thomas, M. H. Brodsky, D. Kaplan, and D. Lepine, Phys. Rev. **B 18**, 3059 (1978).
[4] W. Sinke, T. Warabisako, M. Miyao, T. Tokuyama, S. Roorda, and F.W. Saris, J. Non-Cryst. Solids **99**, 2 (1988).
[5] J. E. Fredrickson, C. N. Waddell, W. G. Spitzer, and G. K. Hubler, Appl. Phys. Lett. **40**, 172 (1982).
[6] K. Laaziri, S. Kycia, S. Roorda, M. Chicoine, J. L. Robertson, J. Wang, and S. C. Moss, Phys. Rev. Lett. **82**, 3460 (1999).
[7] L. de Wit, S. Roorda, W.C. Sinke, F.W. Saris, A.J.M. Berntsen, and W.F. van der Weg, Mat. Res. Soc. Symp. Proc., **205**, 3 (1990).
[8] A. Battaglia, S. Coffa, F. Priolo, G. Campisano, G.A. Baratta, Appl. Phys. Lett. **63**, 2204 (1993).
[9] S. Coffa, F. Priolo, A. Battaglia, Phys. Rev. Lett. **70**, 3756 (1993).
[10] S. Roorda, Nucl. Instr. Meth. B **148**, 366 (1999).
[11] J.-F. Mercure, R. Karmouch, Y. Anahory, S. Roorda, and F. Schiettekatte, Phys. Rev. **B 71**, 134205 (2005).
[12] R. L. C. Vink, G. T. Barkema, and W. F. van der Weg, Phys. Rev. **B 63**, 115210 (2001).
[13] R. Tsu, J.G. Hernandez, and F.H. Pollak , J. Non-Cryst. Solids **66**, 109 (1984).
[14] It could be argued that relaxation state should also be linked to bond length distribution, but at least in the case of *a*-Si produced by self-implantation, this distribution is very narrow, i.e., ~1% of the average bond length [6], leaving only the bond angles as a significant degree of freedom for relaxation.
[15] M. Abernathy, A. Amato, A. Ananyeva, S. Angelova, B. Baloukas, R. Bassiri, G. Billingsley, R. Birney, G. Cagnoli, M. Canepa, M. Coulon, J. Degallaix, A. Di. Michele, M.A. Fazio, M.M. Fejer, D. Forest, C. Gier, M. Granata, A.M. Gretarsson, E.M. Gretarsson, E. Gustafson, E.J. Hough, M. Irving, É. Lalande, C. Lévesque, A.W. Lussier, A. Markosyan, I.W. Martin, L. Martinu, B. Maynard, C.S. Menoni, C. Michel, P.G. Murray, C. Osthelder, S. Penn, L. Pinard, K. Prasai, S. Reid, R. Robie, S. Rowan, B. Sassolas, F. Schiettekatte, R. Shink, S. Tait, J. Teillon, G. Vajente, M. Ward, and L. Yang, Class. Quant. Grav. **38**, 195021 (2021).
[16] X. Liu, M. R. Abernathy, T. H. Metcalf, B. Jugdersuren, J. C. Culbertson, M. Molina-Ruiz, and F. Hellman, Journal of Alloys and Compounds **855**, 157431 (2021).
[17] M. Molina-Ruiz, Y. J. Rosen, H. C. Jacks, M. R. Abernathy, T. H. Metcalf, X. Liu, J. L. DuBois, and F. Hellman, Phys. Rev. Mat. **5**, 035601 (2021).
[18] J. Steinlechner and I. W. Martin, Phys Rev. **D 103**, 042001 (2021).
[19] R. Birney, J. Steinlechner, Z. Tornasi, S. MacFoy, D. Vine, A. S. Bell, D. Gibson, J. Hough,
S. Rowan, P. Sortais, S. Sproules, S. Tait, I. W. Martin, and S. Reid, Phys. Rev. Lett. **121**, 191101 (2018)
[20] D. A. Strubbe, E. C. Johlin, T. R. Kirkpatrick, T. Buonassisi, and J. C. Grossman, Phys. Rev. **B 92**, 241202 (2015).
[21] De Wolf, Semicond. Sci. Technol. **11**, 139 (1995).
[22] Y. B. Gerbig, C. A. Michaels, J. E. Bradby, B. Haberl, R. F. Cook, Phys. Rev. B **92**, 214110 (2015)
[23] J. E. Fredrickson, C. N. Waddell, W. G. Spitzer, and G. K. Hubler, Appl. Phys. Lett. **40**, 172–174 (1982).
[24] M. Delhaye and P. Dhamelincourt, J. Raman Spectrosc. **3** , 1 (1975).
[25] P. Novák, J. Očenášek, L. Prušáková, V. Vavruňková, J. Savková, and J. Rezek, Applied Surface Science **364**, 302 (2016).

[26] E. Gaufrès, S. Marcet, V. Aymong, N. Y-Wa Tang, A. Favron, F. Thouin, C. Allard, D. Rioux, N. Cottenye, M. Verhaegen, and R. Martel, J. Raman Spectrosc. **49**, 174 (2018).
[27] In Ref. 3 the authors show as implanted amorphous silicon at 468 cm^{-1} which is close to our results.
[28] This value is slightly lower than values reported in the literature for fully-relaxed *a*-Si. It could be because the material has not completely relaxed during the first annealing, or it could be a shift due to the temperature, given the high power density. The reference value come from Ref. 5 and it is 478 ± 1 cm^{-1}.
[29] J.F. Ziegler, J.P. Biersack, U. Littmark. *The Stopping and Range of Ions in Solids*. Pergamon Press (1985).
[30] A. Miotello and R. Kelly, Nuclear Instruments and Methods in Physics Research **B 122**, 458-46, (1997).
[31] J.-C. Pothier, F. Schiettekatte, and L.J. Lewis, Phys. Rev. **B 83**, 235206 (2011).
[32] S. Roorda, J.M. Poate, D.C. Jacobson, D.J. Eaglesham, B.S. Dennis, S. Dierker, W.C. Sinke, and F. Spaepen, Solid State Communications **75**, 3, 197-200 (1990).
[33] A. Rowlands, Physics of Digital Photography, IOP Publishing, 2017.
[34] X. Jiang, B. Goranchev, K. Schmidt, P. Grünberg and K. Reichelt, Journal of Applied Physics **67**, 6772–6778 (1990).
[35] D.M. Follstaedt, J.A. Knapp, and S.M. Myers, J. Mater. Res. **19**, 1 (2004).